ChemComm

COMMUNICATION

View Article Online
View Journal | View Issue

Cite this: *Chem. Commun.*, 2024, **60**, 7467

Received 16th April 2024,
Accepted 19th June 2024

DOI: 10.1039/d4cc01798f

rsc.li/chemcomm

Fast-charging aqueous batteries enabled by a three-dimensional ordered Zn anode at deliberate concentration polarization†

Jinze Li,‡[ab] Eryang Mao,‡[c] Xiaozhou Ye,[d] Tian Xu,[b] Jie Zheng,[b] Kaiwen Xiao,[b] Bingbing Sun,[b] Ming Ge,[b] Xiaolei Yuan [b] and Zhao Cai [b] *[a]

A finely controlled concentration polarization environment was deliberately created to fabricate a three-dimensional ordered Zn metal anode with (002)-dominated planes, which enabled a high-rate aqueous Ni–Zn pouch cell with a high discharge capacity of 187.3 mA h g^{-1} at 50 C, and a capacity retention of 94.7% and an average Coulombic efficiency of 99.8% for 500 charge/discharge cycles.

Aqueous Zn batteries (AZBs) appear to have very good prospects for renewable energy storage at grid scale due to their superiority in safety and costs.[1–5] Renewable energy such as wind and tide have intrinsic fluctuation and intermittence, which calls for AZBs with both fast-charging capability and long life-span.[6–8] However, the fast-charging and cycling performance of AZBs have long been restricted by the low reversibility of Zn metal anode materials under high-rate working conditions.[9,10] To improve the sustainability and lifespan of the batteries, significant strategies such as green ether-based and hydrogen bond-regulated electrolytes,[11,12] have been developed. Nevertheless, it is still urgent and challenging to design Zn metal anode materials with both excellent rate and cyclic performance to enable fast-charging aqueous batteries with long life-spans.

One of the major challenges in developing high-rate Zn anodes is the dendrite growth issue during battery charging processes.[13–15] Designing a three-dimensional (3D) Zn electrode with enlarged surface area is an effective way to address such an issue.[16] However, the current methods for achieving 3D Zn anodes including alloying–dealloying and electrodeposition generally involve expensive raw materials (*e.g.* Li or Cu) or produce electrodes with disordered structures (*e.g.* uncontrollable crystal planes).[17,18] More importantly, 3D Zn electrodes with disordered structure typically show uncontrolled Zn plating kinetics and even faster corrosion rates that are proportional to the surface area, which is detrimental to the performance optimization of the 3D Zn electrodes, especially under high-rate working conditions.[19–21] Therefore, it is highly desirable to fabricate 3D Zn anodes with an ordered structure that would suppress dendrites and corrosion side-reactions at the same time, thus enabling fast-charging AZBs.

In this work, a 3D ordered Zn metal anode was fabricated *via* finely controlled electrodeposition with deliberate concentration polarization (hereafter denoted as 3DZn@CP). By employing low concentration electrolyte and ensuring the concentration polarization on the electrode surface, the 3DZn@CP anode exhibited a 13.2 times larger surface area, thus lowering the Zn plating nucleation barrier and suppressing the dendrite formation. Simultaneously, by applying a deposition current density lower than the activation current density for the growth of high-index planes of metallic Zn, the 3DZn@CP anode produced a thermodynamically stable (002)-dominated surface structure, thus showing an excellent anti-corrosion performance with 50 mV higher corrosion potential and 2.7 mA cm^{-2} lower corrosion current density compared with a commercial Zn anode. Consequently, the 3DZn@CP electrode showed a low overpotential of 21 and 97 mV at 1 and 20 mA cm^{-2}, respectively, 16 and 325 mV lower than the commercial Zn counterpart. Moreover, the aqueous Ni–3DZn@CP full cells displayed an excellent rate performance with a high capacity of 183.2 mA h g^{-1} under an extremely high rate of 50 C, which remained at 97.7% of its initial capacity after 2000 cycles, outperforming the Ni–Zn cells (113.4 mA h g^{-1}, remained at 62.1% after 200 cycles at 50 C) and most fast-charging AZBs in recent publications. These results pave a new

[a] *Faculty of Materials Science and Chemistry, China University of Geosciences, Wuhan 430074, China. E-mail: caizhao@cug.edu.cn*
[b] *School of Chemistry and Chemical Engineering, Nantong University, Nantong 226019, China*
[c] *State Key Laboratory of Catalysis, Dalian National Laboratory for Clean Energy, Dalian Institute of Chemical Physics, Chinese Academy of Sciences, Dalian 116023, China*
[d] *The Second Research Department, Shanghai Institute of Satellite Engineering, Shanghai 201109, China*

† Electronic supplementary information (ESI) available. See DOI: https://doi.org/10.1039/d4cc01798f

‡ These authors contributed equally to this work.

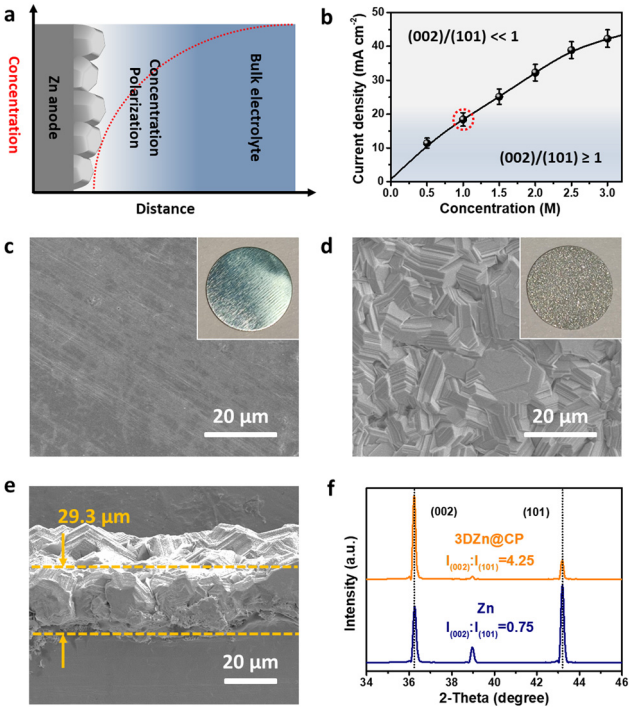

Fig. 1 (a) Schematic illustration of the Zn metal electrodeposition under concentration polarization. (b) The limiting current densities for concentration polarization during Zn electrodeposition with different electrolyte concentrations based on Sand's model. Top-view SEM images of the (c) pristine Zn and (d) 3DZn@CP electrodes, the insets show the digital images of the corresponding electrodes. (e) Cross-section SEM image of the 3DZn@CP electrode. (f) XRD analysis of the pristine Zn and 3DZn@CP electrodes.

way to construct 3D Zn electrodes with ordered surface structure for next-generation fast-charging aqueous batteries.

Concentration polarization generally leads to the exhaustion of Zn^{2+} ions near the electrode surface and the formation of porous Zn deposits (Fig. 1a). Limiting current density for concentration polarization during Zn deposition with different electrolyte concentrations was first studied based on Sand's model. As shown in Fig. 1b, with the increasing $ZnSO_4$ concentration from 0.5 to 3.0 M, the limiting current density increased from 14.3 to 52.9 mA cm^{-2}, respectively. These results suggest adopting high current densities to electrodeposit Zn anodes with high porosity and large surface area. Also to be noted is that low current density conditions are beneficial for the growth of low-index crystal planes such as (002). High current densities would activate the growth of high-index planes for Zn. In a typical case, the (002)/(101) ratio of Zn deposits was greater than 1 with the current density lower than ~20 mA cm^{-2}.[22] Taking these factors together, we combined an electrolyte concentration of 1 M and a deposition current density of 20 mA cm^{-2} to fabricate a Zn electrode with high porosity and a (002)-dominated surface. While the commercial Zn electrode showed a flat and compact surface (Fig. 1c and Fig. S1, ESI†), the as-deposited 3DZn@CP electrode exhibited a stacked hexagonal crystal morphology (Fig. 1d and Fig. S2, ESI†). Note that the pristine Zn showed a clear metallic luster based on mirror reflectance. In contrast, the 3DZn@CP electrode exhibited a uniform diffuse reflectance by the naked eye (insets in Fig. 1c and d), suggesting an ordered micro-surface structure. The thickness of the deposited Zn was determined to be 29.3 μm (Fig. 1e), suggesting a porosity of 58.1%. Moreover, the plane ratio between (002) and (101) for the 3DZn@CP electrode was 4.25 based on XRD analysis (Fig. 1f and Fig. S3, ESI†), much higher than the pristine Zn (0.75), further confirming the (002)-dominated surface for the as-achieved 3DZn@CP electrode. In addition, the deposited Zn electrode in the same 1 M $ZnSO_4$ but with a higher current density of 50 mA cm^{-2} showed a non-uniform disordered structure with randomly stacked Zn plates (Fig. S4, ESI†), indicating a (002)-dominated surface with much higher porosity. These results in turn demonstrate the importance of fine control of the concentration polarization to prepare the 3D ordered Zn metal electrode.

The 3DZn@CP electrode exhibited an enlarged surface area, which was studied by measuring the double layer capacity based on electrochemical impedance spectroscopy (EIS).[23] As shown in Fig. 2a and b, the 3DZn@CP electrode showed a double layer capacity of 38.4 μF cm^{-2}, an order of magnitude higher than that of the commercial Zn electrode (2.7 μF cm^{-2}). Moreover, the 3DZn@CP electrode displayed a charge transfer resistance of 24 Ω, much smaller than the commercial Zn (56 Ω). While the commercial Zn showed a large nucleation

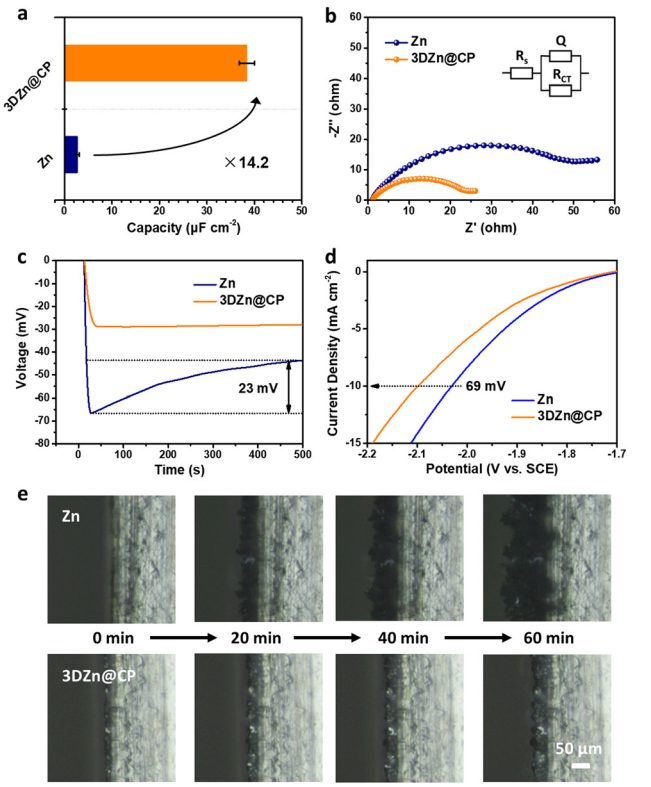

Fig. 2 (a) The electrical double-layer capacitance analysis, (b) EIS plots, (c) voltage–time curves during Zn nucleation at 1 mA cm^{-2} and (d) hydrogen evolution linear polarization curves of commercial Zn and 3DZn@CP electrodes. (e) Cross-section OM images of the Zn and 3DZn@CP electrodes during Zn plating at 20 mA cm^{-2}.

overpotential of 23 mV during Zn plating at 1 mA cm^{-2}, the 3DZn@CP electrode displayed a stable voltage response during the whole plating process with no nucleation overpotential (Fig. 2c), indicating a uniform plating behavior. The plating current density of the 3DZn@CP electrode at −100 mV became stable within 42 s, a much shorter time than the commercial Zn (115 s, Fig. S5, ESI†); the constrained 2D diffusion of the 3DZn@CP electrode should also be beneficial for the uniform Zn plating. In addition, since (002) is the most thermodynamically stable plane for hexagonal Zn metal, the 3DZn@CP electrode with a (002)-dominated surface structure should have excellent corrosion resistance. As shown in Fig. S6 (ESI†), while a similar shape is observed for the two corrosion linear polarization curves of Zn and 3DZn@CP electrodes, the corrosion potential of the 3DZn@CP electrode shifted to be more anodic, from −1.06 V to −1.01 V compared with the commercial Zn electrode. The corrosion current density of the 3DZn@CP electrode determined by the Tafel fit turned out to be 0.28 mA cm^{-2}, much smaller than the commercial Zn (0.55 mA cm^{-2}). Moreover, the overpotential of the 3DZn@CP electrode at the hydrogen evolution current density of 10 mA cm^{-2} was 69 mV lower than the commercial Zn based on the hydrogen evolution polarization curves in Fig. 2d, demonstrating the improved anti-corrosion performance of the as-achieved 3DZn@CP electrode. Since the 3DZn@CP electrode exhibited a lower Zn nucleation overpotential and suppressed corrosion/hydrogen evolution side-reactions compared with commercial Zn, the plating/stripping behavior of the 3DZn@CP electrode should be more uniform. As the optical microscope (OM) images show in Fig. 2e, the Zn electrode showed a loose deposition during the whole plating process at 20 mA cm^{-2} for 60 min. In sharp contrast, the Zn plating on the 3DZn@CP electrode was significantly denser with a clear metallic luster, suggesting uniform Zn deposition, which should be beneficial for the dendrite-free performance of the as-designed 3DZn@CP electrode.

The uniform Zn plating and anti-corrosion behavior should improve the electrochemical performance of the 3DZn@CP electrodes under high rate working conditions, which was first studied in Zn‖Zn and 3DZn@CP‖3DZn@CP symmetrical cells. As shown in Fig. 3a, the 3DZn@CP electrode displayed overpotentials of 21, 35, 56, and 97 mV at 1, 5, 10, and 20 mA cm^{-2}, respectively, much lower than the commercial Zn electrode (37, 122, 223, and 422 mV) under the same test conditions. At the current density of 1 mA cm^{-2} and areal capacity of 0.5 mA h cm^{-2}, the 3DZn@CP electrode displayed a long cycle-life of 800 h, superior to the commercial Zn electrode (78 h, Fig. S7, ESI†). At the high current density of 20 mA cm^{-2} and high areal capacity of 10 mA h cm^{-2}, the 3DZn@CP electrode cycled stably for 100 h (Fig. 3b and c). In contrast, the commercial Zn electrode showed large voltage fluctuations, and a clear short circuit could be observed at the 22^{th} electrochemical cycle, implying the real possibility of dendrite formation. SEM studies further revealed that Zn metal was uniformly plated on the 3DZn@CP electrode at 20 mA h cm^{-2} (Fig. S8, ESI†); the commercial Zn electrode showed nonuniform Zn deposition behavior under the same plating conditions

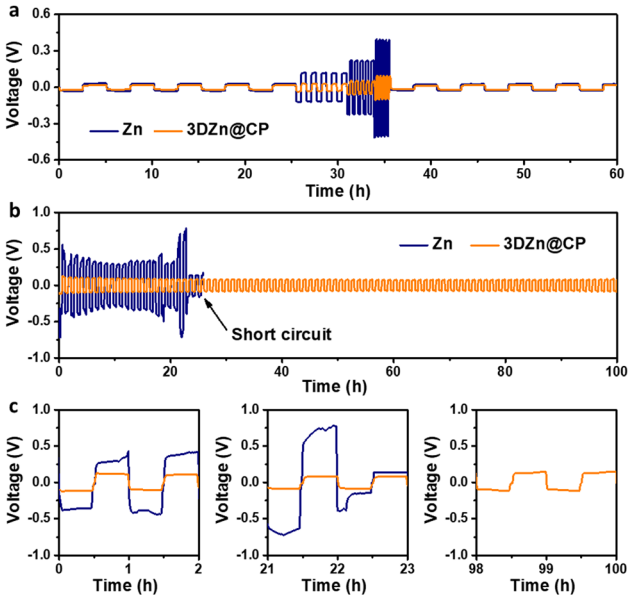

Fig. 3 (a) Rate performance of Zn‖Zn and 3DZn@CP‖3DZn@CP symmetrical cells at 1, 5, 10, 20 mA cm^{-2} with a fixed areal capacity of 2.5 mA h cm^{-2}. (b) Voltage profiles and (c) enlarged voltage profiles of the specific cycles for Zn‖Zn and 3DZn@CP‖3DZn@CP symmetrical cells at 20 mA cm^{-2} and 10 mA h cm^{-2}.

(Fig. S9, ESI†), further demonstrating the suppressed Zn dendrite formation on the 3DZn@CP electrode under high current densities.

The rate performance and reversibility of the 3DZn@CP electrode were further investigated in both coin and pouch cell configurations with commercial $Ni(OH)_2$ cathodes. As shown in Fig. 4a and Fig. S10 (ESI†), while the $Ni(OH)_2$‖Zn (Ni–Zn) and $Ni(OH)_2$‖3DZn@CP (Ni–3DZn@CP) coin cells exhibited similar redox behavior, the polarization voltage of the Ni–3DZn@CP coin cell was 46 mV lower than that of the Ni–Zn coin cell, suggesting the improved reversibility of the 3DZn@CP electrode. The improved reversibility of the 3DZn@CP electrode was also confirmed in Zn‖Ti half cells. As shown in Fig. S11 (ESI†), the 3DZn@CP‖Ti cell showed a higher Coulombic efficiency of 99.6% than the Zn‖Ti cell (91.4%) at 2 mA cm^{-2} and 0.5 mA h cm^{-2}. Moreover, the Ni–3DZn@CP coin cell showed a charge transfer resistance of 28 Ω, much smaller than the Ni–Zn coin cell (89 Ω, Fig. S12, ESI†). The Ni–3DZn@CP coin cell displayed reversible capacities of 226.7, 211.6, 195.5, and 183.2 mA h g^{-1} at the current densities of 1, 5, 10, 50 C, respectively, much higher than the Ni–Zn (218.8, 186.6, 157.6, and 113.4 mA h g^{-1}, Fig. 4b). In addition, the Ni–3DZn@CP coin cell exhibited a high capacity retention of 97.7% with an average Coulombic efficiency (CE) of 99.9% after 2000 cycles at 50 C, outperforming the Ni–Zn coin cell (capacity retention of 62.1% after 200 cycles, CE of 99.1%) and most fast-charging aqueous batteries in recent publications (Fig. 4c and Table S1, ESI†). Note that the commercial Zn electrode in Ni–Zn coin cells showed severe deformation after 200 cycles at 50 C, but the 3DZn@CP electrode maintained its initial circular shape (Fig. S13, ESI†), indicating the high anti-deformation

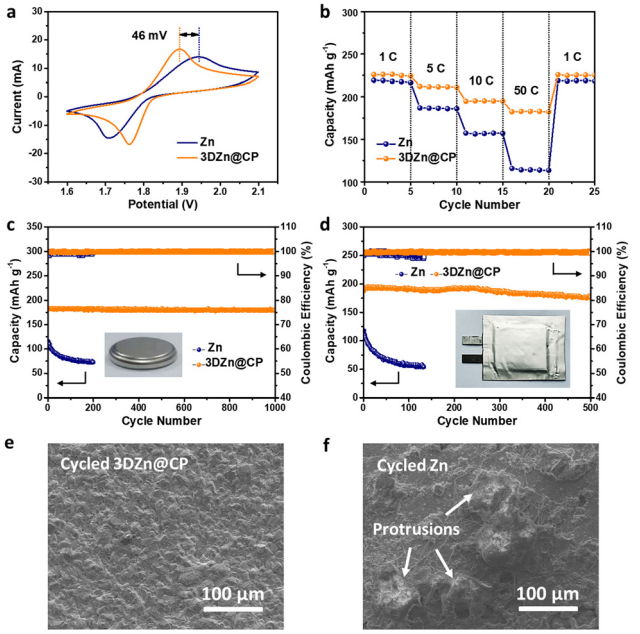

Fig. 4 (a) CV profiles, (b) rate performance, and (c) cycling performance at 50 C of the Ni–Zn and Ni–3DZn@CP coin cells. (d) Cycling performance at 50 C of the Ni–Zn and Ni–3DZn@CP pouch cells. The insets in (c) and (d) demonstrate the as-assembled coin and pouch cells, respectively. SEM images of the (e) 3DZn@CP and (f) commercial Zn electrodes after full pouch cell cycling at 50 C.

ability. More impressively, the Ni–3DZn@CP pouch cell also exhibited remarkable cycling stability with 94.7% capacity retention after 500 charge/discharge cycles at 50 C, superior to the Ni–Zn pouch cell (only 45.1% after 100 cycles) under the same test conditions (Fig. 4d). The 3DZn@CP electrode exhibited a relatively planar and uniform surface after 100 cycles at 50 C (Fig. 4e), in sharp contrast with the pristine Zn with rugged surface morphology (Fig. 4f), further suggesting the enhanced reversibility of the 3DZn@CP electrode under high-rate working conditions.

In summary, a finely controlled concentration polarization environment was deliberately created to electrodeposit a 3D ordered Zn metal anode. The 3DZn@CP electrode exhibited an order of magnitude larger surface area and dendrite-free Zn plating behavior at high current densities up to 20 mA cm^{-2}. Moreover, the 3DZn@CP electrode with a (002)-dominated surface showed improved anti-corrosion performance (−1.01 V, 0.28 mA cm^{-2} for 3DZn@CP and −1.06 V, 0.55 mA cm^{-2} for Zn). As a result, the 3D@Zn electrode showed a low overpotential of 97 mV at 20 mA cm^{-2} and 10 mA h cm^{-2} in a symmetrical cell configuration and a stable cycling performance with an initial capacity of 183.2 mA h g^{-1} and a high capacity retention of 97.7% after 2000 cycles at an extremely high rate of 50 C in a full cell configuration. These results not only demonstrate deliberate concentration polarization as an effective way for fabricating 3D Zn anodes with ordered electrode structures, but also suggest the importance of achieving a high-rate and reversible Zn anode for enabling fast-charging aqueous batteries with long life-spans.

This work was financially supported by the National Natural Science Foundation of China (No. 22205068), the "CUG Scholar" Scientific Research Funds at China University of Geosciences (Wuhan) (Project No. 2022118), and the Postdoctoral Fellowship Program of CPSF under Grant Number GZC20232578.

Data availability

Data supporting the findings of this study are available from the corresponding author upon reasonable request.

Conflicts of interest

There are no conflicts to declare.

Notes and references

1 D. Han, C. Cui, K. Zhang, Z. Wang, J. Gao, Y. Guo, Z. Zhang, S. Wu, L. Yin, Z. Weng, F. Kang and Q.-H. Yang, *Nat. Sustain.*, 2022, **5**, 205–213.
2 M. Xi, Z. Liu, W. Wang, Z. Qi, R. Sheng, J. Ding, Y. Huang and Z. Guo, *Energy Environ. Sci.*, 2024, **17**, 3168–3178.
3 Y. Zhou, C. Li, Y. Zhang, L. Wang, X. Fan, L. Zou, Z. Cai, J. Jiang, S. Zhou, B. Zhang, H. Zhang, W. Li and Z. Chen, *Adv. Funct. Mater.*, 2023, **33**, 2304302.
4 Z. Wang, M. Zhou, L. Qin, M. Chen, Z. Chen, S. Guo, L. Wang, G. Fang and S. Liang, *eScience*, 2022, **2**, 209–218.
5 X. Fan, Z. Chen, D. Xu, L. Zou, F. Ouyang, S. Deng, X. Wang, J. Zhao and Y. Zhou, *Adv. Funct. Mater.*, 2024, 2404750.
6 J. Wang, B. Zhang, Z. Cai, R. Zhan, W. Wang, L. Fu, M. Wan, R. Xiao, Y. Ou, L. Wang, J. Jiang, Z. W. Seh, H. Li and Y. Sun, *Sci. Bull.*, 2022, **67**, 716–724.
7 G. Li, X. Duan, X. Liu, R. Zhan, X. Wang, J. Du, Z. Chen, Y. Li, Z. Cai, Y. Shen and Y. Sun, *Adv. Mater.*, 2023, **35**, 2207310.
8 S. Chen, S. R. Jeong and S. Tao, *Mater. Rep. Energy*, 2022, **2**, 100096.
9 Y. Guo, R. Zhang, S. Zhang and C. Zhi, *Nano Mater. Sci.*, 2022, DOI: 10.1016/j.nanoms.2022.09.004.
10 F. Bu, Y. Gao, W. Zhao, Q. Cao, Y. Deng, J. Chen, J. Pu, J. Yang, Y. Wang, N. Yang, T. Meng, X. Liu and C. Guan, *Angew. Chem., Int. Ed.*, 2024, **63**, e202318496.
11 M. Xia, H. Fu, K. Lin, A. M. Rao, L. Cha, H. Liu, J. Zhou, C. Wang and B. Lu, *Energy Environ. Sci.*, 2024, **17**, 1255–1265.
12 X. Ma, H. Fu, J. Shen, D. Zhang, J. Zhou, C. Tong, A. M. Rao, J. Zhou, L. Fan and B. Lu, *Angew. Chem., Int. Ed.*, 2023, **62**, e202312973.
13 L. Li, S. Jia, M. Cao, Y. Ji, H. Qiu and D. Zhang, *Rare Met.*, 2024, **43**, 20–40.
14 J. Li, D. Röhrens, G. Dalfollo, X. Wu, Z. Lu, Q. Gao, B. Han, R. Sun, C. Zhou, J. Wang and Z. Cai, *Nano Mater. Sci.*, 2023, DOI: 10.1016/j.nanoms.2023.11.004.
15 Y. Ou, Z. Cai, J. Wang, R. Zhan, S. Liu, Z. Lu and Y. Sun, *EcoMat*, 2021, **4**, e12167.
16 P. Ruan, X. Chen, L. Qin, Y. Tang, B. Lu, Z. Zeng, S. Liang and J. Zhou, *Adv. Mater.*, 2023, **35**, 2300577.
17 R. Xiao, Z. Cai, R. Zhan, J. Wang, Y. Ou, Z. Yuan, L. Wang, Z. Lu and Y. Sun, *Chem. Eng. J.*, 2021, **420**, 129642.
18 X. Wang, C. Han, S. Dou and W. Li, *Nano Mater. Sci.*, 2022, DOI: 10.1016/j.nanoms.2022.10.004.
19 Z. Cai, Y. Ou, J. Wang, R. Xiao, L. Fu, Z. Yuan, R. Zhan and Y. Sun, *Energy Storage Mater.*, 2020, **27**, 205–211.
20 H. Tian, J.-L. Yang, Y. Deng, W. Tang, R. Liu, C. Xu, P. Han and H. J. Fan, *Adv. Energy Mater.*, 2023, **13**, 2202603.
21 Z. Cai, J. Wang and Y. Sun, *eScience*, 2023, **3**, 100093.
22 Z. Cai, J. Wang, Z. Lu, R. Zhan, Y. Ou, L. Wang, M. Dahbi, J. Alami, J. Lu, K. Amine and Y. Sun, *Angew. Chem., Int. Ed.*, 2022, **61**, e202116560.
23 J. Wang, Z. Cai, R. Xiao, Y. Ou, R. Zhan, Z. Yuan and Y. Sun, *ACS Appl. Mater. Interfaces*, 2020, **12**, 23028–23034.

